Climatological baroclinic forcing of the barotropic flow in the East Greenland Current in Fram Strait

Pawel Schlichtholz

Institute of Oceanology, Polish Academy of Sciences, Sopot, Poland

Received 7 September 2004; revised 24 March 2005; accepted 23 May 2005; published 26 August 2005.

[1] Baroclinic forcing of the barotropic flow in the East Greenland Current in Fram Strait (EGC_{FS}) is studied using theoretical analysis and climatological data. First, the validity of the arrested topographic wave (ATW) vorticity balance is reexamined. Then, a distribution of the net (depth-averaged) relative geostrophic flow and the associated along-isobath variations of the bottom density are estimated from the Polar Science Center Hydrographic Climatology (Seattle, Washington, United States). The effect of the along-isobath bottom density variations is referred to as $JEBAR_b$ in order to distinguish it from the famous JEBAR (joint effect of baroclinicity and relief), which involves depth-integrated density variations. It is shown that the $JEBAR_b$ is able to maintain a significant bottom geostrophic flow in the climatological EGC_{FS}. Estimates of the $JEBAR_b$ at 79°N correspond to an increase of the magnitude of the flow by $\sim$3 cm s^{-1} over a distance of 200 km along the continental slope. An analytical solution for the flow that is driven by a constant $JEBAR_b$ term and satisfies the ATW vorticity balance is then obtained in a domain bounded by two parallel isobaths. Finally, the $JEBAR_b$ is related to the JEBAR. It is shown that while the $JEBAR_b$ maintains the curl of the Coriolis force associated with the bottom geostrophic flow, the JEBAR maintains the curl of the net Coriolis force associated with the absolute geostrophic flow. In the climatological EGC_{FS} over the continental slope, the JEBAR is nearly equal to the $JEBAR_b$.

Citation: Schlichtholz, P. (2005), Climatological baroclinic forcing of the barotropic flow in the East Greenland Current in Fram Strait, *J. Geophys. Res.*, *110*, C08013, doi:10.1029/2004JC002701.

1. Introduction

[2] A forced-planetary vorticity balance often invoked in the theories of the large-scale flow in a flat-bottomed ocean is the Sverdrup balance, i.e., a balance between the vortex tube squashing by the surface Ekman pumping and the advection of planetary vorticity by the geostrophic transport [e.g., *Pedlosky*, 1996]. On the other hand, a geostrophic flow over a sloping bottom in an area with a small variation of the Coriolis parameter is likely to be in a vorticity balance between the bottom Ekman pumping and the vortex tube stretching by the cross-isobath bottom geostrophic flow. The motion associated with such a frictional-topographic vorticity balance is often referred to as the arrested topographic wave (ATW). The original ATW model was constructed by *Csanady* [1978] from steady equations for a net (depth-averaged), wind-driven flow in a coastal zone. Various formulations of the ATW exist. A common feature of the ATW models is that the bottom stress is assumed to be proportional to a velocity. Another assumption is that only the along-isobath component of bottom friction is dynamically relevant, while the bottom topography is simplified to be a plane sloping in one direction (Figure 1). The model equations can then be combined into a parabolic equation for a single variable which, for a constant bottom slope, is an analog of the one-dimensional equation for heat conduction. A general, nondimensional form of the equation for a variable $\mathcal{A}$ is

$$\frac{\partial^2 \mathcal{A}}{\partial x^2} + \frac{\partial \mathcal{A}}{\partial y} + Q = 0, \tag{1}$$

where x and y are the cross- and along-isobath coordinates, respectively. Negative of y plays the role of time in the heat conduction analogy, while the term Q is a "source" function depending on the problem at hand. For instance, Csanady's original model resulted in a homogeneous ($Q = 0$) equation for the surface elevation. The author also considered the problem of freshwater influx at the shore, in which a nonhomogeneous term ($Q \neq 0$) appears in the governing equation [*Csanady*, 1978]. A nonhomogeneous term also appears in the governing equation of other ATW models for flow in a baroclinic ocean. It appears, for instance, in an equation for the along-isobath component of the bottom geostrophic velocity, v_{gb}, derived by *Shaw and Csanady* [1983]. The equation for v_{gb} was recently used by *Schlichtholz* [2002] to interpret the bottom geostrophic flow over the continental slope in the East Greenland Current in Fram Strait (EGC_{FS}) using hydro-

0148-0227/05/2004JC002701$09.00

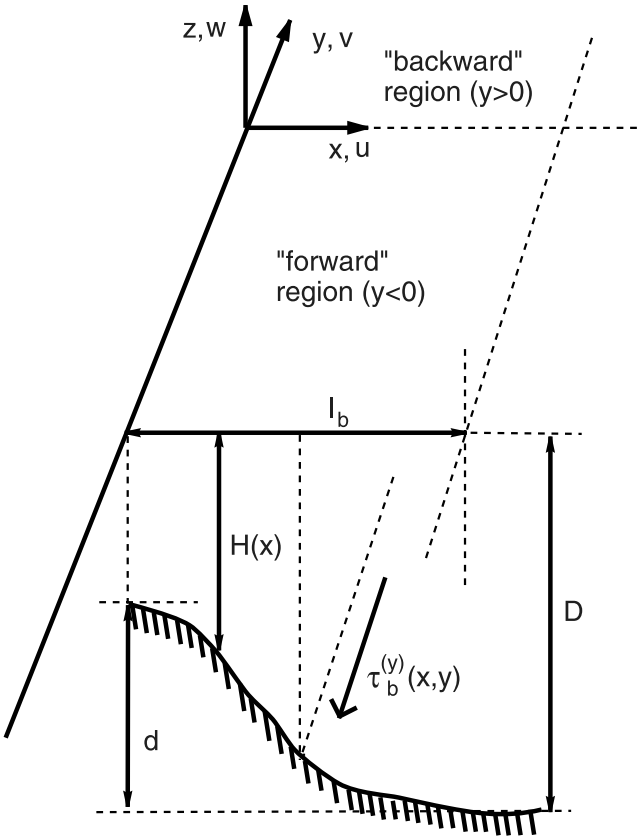

Figure 1. Schematic representation of the geometry used in the arrested topographic wave models. Symbols are explained in the text. Two essential simplifications are that the bottom depth slopes only in one direction and that only the along-isobath component of the bottom stress is important. Here, the stress vector corresponds to a flow in the direction of propagation of the topographic Rossby waves, i.e., with the shallower water to the right when looking downstream, as in the East Greenland Current. A further simplification is to prescribe a uniform bottom slope, so that a closed equation for some flow variables becomes analogous to the one-dimensional equation for heat conduction (see equation (1)). An analytical solution of that equation for the bottom geostrophic flow in a domain between two isobaths is presented in Figure 12.

graphic data from summer 1984 (MIZEX 84 data) and an inverse model based on these data [*Schlichtholz and Houssais*, 1999a].

[3] The southward flow in the EGCFS (Figure 2) is an important element of the current system in the Arctic Mediterranean. Not only it evacuates sea ice and fresh surface polar water from the Arctic Ocean, but it is also a means by which intermediate and deep waters from that ocean can get to the Nordic Seas [e.g., *Aagaard et al.*, 1985; *Rudels et al.*, 1999]. An outflow of these waters occurs along the East Greenland Slope. In addition to water masses advected from the Arctic Ocean along the continental slope, the EGCFS receives some water masses locally in Fram Strait, mainly through westward recirculations of Atlantic and deep waters from the West Spitsbergen Current, and also through injection of surface polar water along the East Greenland Polar Front (Figure 2). Local admixtures gradually change the water mass characteristics along the slope [e.g., *Schlichtholz and Houssais*, 1999b, 2002]. Along-isobath gradients of density are present in the EGCFS near the bottom, as shown by *Schlichtholz* [2002], and generally in the whole water column, as demonstrated by *Schlichtholz and Houssais* [1999c] using distributions of potential energy calculated from the MIZEX 84 data. The along-isobath density gradients are dynamically important since they do not only determine the vertical shear of the cross-isobath component of the geostrophic flow, but also constitute a driving agent for the barotropic flow. The along-isobath variations of the bottom density appear in a formula for the divergence of the bottom geostrophic flow derived by *Shaw and Csanady* [1983]. The formula, when combined with the ATW vorticity balance, gives rise to the "source" term in equation (1) for $\mathcal{A} = v_{gb}$. On the other hand, the along-isobath variations of potential energy appear in the famous JEBAR (joint effect of baroclinicity and relief) term in the vorticity balance for the net flow. The JEBAR effect was introduced to oceanography by *Sarkisyan and Ivanov* [1971] and interpreted in terms of a cross-isobath net baroclinic flow by *Mertz and Wright* [1992]. Its diagnosis from the MIZEX 84 data gave rise to an analytical model of the EGCFS in which the JEBAR term was balanced by a damping term due to either bottom or internal friction [*Schlichtholz and Houssais*, 1999c]. That model was the first attempt to explain the barotropic flow in the EGCFS as resulting from local baroclinic influences over a sloping bottom. The subsequent study of *Schlichtholz* [2002] made it clear that, on the assumption of geostrophy, the bottom flow in the current should be maintained by the effect of along-isobath variations of the bottom density. The effect can be referred to as JEBAR$_b$ (joint effect of bottom baroclinicity and relief) in order to stress the fact that it involves baroclinicity at the ocean bottom instead of a total (depth-integrated) baroclinicity.

[4] The present study is intended to give further insight into the dynamics of the EGCFS and tackles, after an introduction of basic equations in section 2, with four problems. The first problem concerns the validity of the ATW balance which is checked in section 3 against observations reported in the literature. The second problem concerns the persistence of the JEBAR$_b$. Till now only the importance of that effect for maintaining the flow in summer 1984 has been evidenced. In section 4, the effect is quantified using climatological data. A short discussion of a relationship between the along-isobath bottom density variations and the distribution of the baroclinic transport is included in that section. Errors of the climatological fields are discussed in Appendix A. The third problem is whether an analytical solution to equation (1) can grasp main features of the bottom flow in the EGCFS. An approximate solution for v_{gb} when $Q = const$, analogous to the solution for the surface elevation in Csanady's problem of freshwater influx at the shore, was mentioned by *Schlichtholz* [2002]. That solution is a part of a solution in a domain which is semi-infinite in both x and y [*Csanady*, 1978]. Here, in section 5, exact solutions are obtained in a domain bounded in x (Figure 1). The fourth problem, discussed in section 6, concerns a relationship

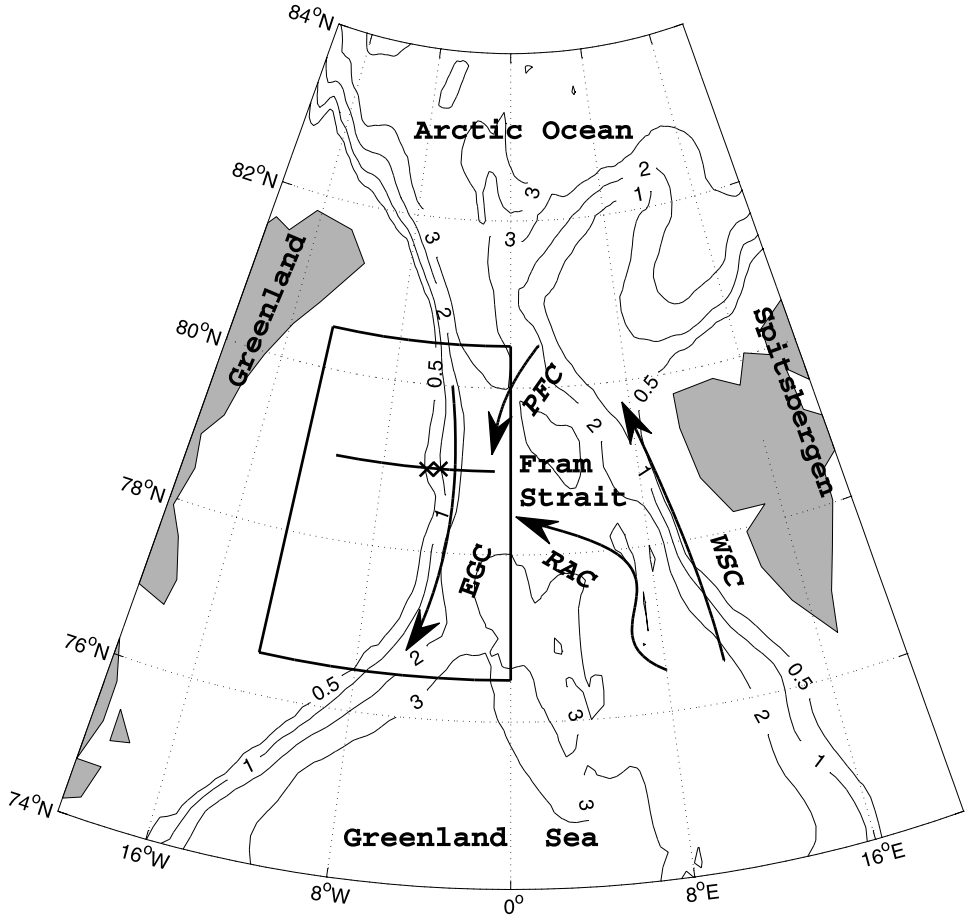

Figure 2. Topography of Fram Strait (in kilometers). The box on the western side of the strait encompasses the area for which distributions of some climatological variables are presented in Figures 3, 6–8, and 10. The bold line within the box at 79°N indicates the position of the section at which some other variables are plotted in Figures 9, 11, and 13. The crosses on that section approximately correspond to the locations of moorings FS-1 and FS-2 from *Foldvik et al.* [1988]. The arrows are schematic representation of the currents in Fram Strait. Acronyms are as follows: EGC, East Greenland Current; PFC, Polar Front Current; RAC, Return Atlantic Current; and WSC, West Spitsbergen Current.

between the $JEBAR_b$ and JEBAR in general, and in the EGCFS in particular.

2. Large-Scale Dynamics

[5] The "large-scale" approximations to the horizontal momentum equation and the mass conservation equation are

$$f\hat{\mathbf{z}}\times\mathbf{u}=\frac{1}{\rho_0}\left(-\nabla p+\frac{\partial\boldsymbol{\tau}}{\partial z}\right), \tag{2}$$

$$\nabla\cdot\mathbf{u}+\frac{\partial w}{\partial z}=0, \tag{3}$$

where $\mathbf{u}$ is the horizontal velocity vector, w is the velocity component in the z (vertical) direction parallel to the local direction of gravity (positive upward), $\hat{\mathbf{z}}$ is a vertical unit vector, p is the pressure, ρ_0(= 1027 kg m^{-3}) is a reference density, ∇ is the horizontal gradient operator, f is the Coriolis parameter, and $\boldsymbol{\tau}$ is the vertical shearing stress. The stress is significant only in thin boundary layers. In the ocean interior, equation (2) is reduced to the balance between the Coriolis acceleration and the horizontal pressure gradient, i.e.,

$$f\hat{\mathbf{z}}\times\mathbf{u}_g=-\frac{\nabla p}{\rho_0}, \tag{4}$$

where the index g stresses the fact that the horizontal flow is geostrophic.

[6] In a homogeneous ocean the geostrophic velocity is depth-independent while in a nonhomogenous ocean a vertical shear of $\mathbf{u}_g$ appears because the vertical pressure gradient is related to the density, ρ, by

$$\frac{\partial p}{\partial z}=-g\rho, \tag{5}$$

where g(= 9.8 m s^{-2}) is the gravitational acceleration. Eliminating the pressure between the geostrophic equation (4) and the hydrostatic equation (5) yields the famous thermal wind relation. Consequently, the absolute geostrophic velocity at any depth level can be

decomposed into a depth-independent bottom contribution, $\mathbf{u}_{gb}$, and a contribution relative to the bottom, $\mathbf{u}_{gr}$, i.e.,

$$\mathbf{u}_g = \mathbf{u}_{gb} + \mathbf{u}_{gr}. \tag{6}$$

The relative velocity is entirely determined by the density distribution below the given level,

$$\mathbf{u}_{gr} = \frac{g}{f\rho_0}\int_{-H}^{z} \hat{\mathbf{z}} \times \nabla\rho dZ, \tag{7}$$

where H is the bottom depth.

[7] The bottom geostrophic flow should be determined, at least partly, by the vertical boundary conditions, and hence the barotropic vorticity equation. Appropriate kinematic conditions for equation (3) are those of no-normal flow,

$$w|_{z=0} \equiv w_s = 0, \tag{8}$$

$$w|_{z=-H} \equiv w_b = -\mathbf{u}_b \cdot \nabla H, \tag{9}$$

where the indices s and b denote evaluation at the ocean surface and bottom, respectively. The corresponding dynamical boundary conditions for equation (2) are

$$\boldsymbol{\tau}|_{z=0} = \boldsymbol{\tau}_s, \tag{10}$$

$$\boldsymbol{\tau}|_{z=-H} \equiv \boldsymbol{\tau}_b = r\rho_0 \mathbf{u}_{gb}, \tag{11}$$

where $\boldsymbol{\tau}_s$ is the wind stress, while r is a constant friction coefficient with dimension of velocity.

[8] Following one of the procedures outlined by, e.g., *Mertz and Wright* [1992], the barotropic vorticity equation associated with equations (2), (3), and (8)–(11) can be written as

$$-fw_{Es} + H\overline{\mathbf{u}}_g \cdot \nabla f - f\mathbf{u}_{gb} \cdot \nabla H + rf\hat{\mathbf{z}} \cdot \nabla \times \left(\frac{\mathbf{u}_{gb}}{f}\right) = 0, \tag{12}$$

where the overbar denotes vertical averaging from the surface to the bottom, and w_{Es} is the surface Ekman pumping velocity,

$$w_{Es} = \hat{\mathbf{z}} \cdot \nabla \times \left(\frac{\boldsymbol{\tau}_s}{f\rho_0}\right). \tag{13}$$

With the last two terms on the left-hand side (LHS) neglected, equation (12) is reduced to the Sverdrup balance, while with the first two terms neglected, it becomes the ATW balance. In the diagnostic context, equation (12) is an equation for $\mathbf{u}_{gb}$ whatever is the actual local balance since $\overline{\mathbf{u}}_g = \mathbf{u}_{gb} + \overline{\mathbf{u}}_{gr}$. When the friction term is neglected, the resulting hyperbolic problem can easily be solved for the flow field [e.g., *Bogden et al.*, 1993]. With the friction term included, the problem becomes parabolic. The inverse modeling applied by *Schlichtholz and Houssais* [1999a] to the MIZEX 84 data is an example of an attempt to solve that problem in a variational manner.

3. Vorticity Balance

[9] The relative magnitude of the four terms in equation (12) can be expressed as

$$W_s : W_\beta : W_t : W_f = W_s : \frac{\beta_c D V_\beta}{f_c} : s_0 U_b : \frac{r V_b}{f_c l_b}, \tag{14}$$

where W_s, W_β, W_t, and W_f are the scales of the surface Ekman suction, "equivalent vertical velocity" due to the meridional geostrophic transport, vertical velocity induced by the cross-isobath bottom geostrophic flow, and bottom Ekman pumping, respectively. The last three scales have been defined using the scales of the Coriolis parameter and its gradient, f_c and β_c, respectively, the scales of the ocean depth and bottom slope, D and s_0, respectively, the scales of the cross- and along-isobath components of the bottom geostrophic flow, U_b and V_b, respectively, the associated cross-isobath length scale of motion, l_b, and the scale of the meridional component of the net geostrophic flow, V_β.

[10] All scales on the LHS of equation (14) but W_s depend on estimates of the horizontal velocity components. Since the isobaths in the area of the EGCFS nearly coincide with the meridians (Figure 2), we can assume that the along-isobath and meridional flows have a same scale. The magnitude of the near-bottom flow in the EGCFS is on the order of a few centimeters per second, as shown by *Foldvik et al.* [1988] from yearlong current meter measurements at 79°N starting in the period of the MIZEX 84 experiment. The annual mean speed from the deepest instruments at their moorings FS-1 and FS-2 located on the East Greenland Slope (Figure 2) was ~2.5 cm s^{-1}. The deep instruments were placed 25 m and 300 m above the bottom, over the isobaths $H_{FS\text{-}1} \approx 1100$ m and $H_{FS\text{-}2} \approx 1700$ m, respectively. That a typical magnitude of the deep flow in the EGCFS is 2–3 cm s^{-1} seems to be corroborated by recent current measurements. Figure 4 of *Fahrbach et al.* [2001] shows a vertical transect of the meridional velocity component in Fram Strait at 79°N averaged over the period from September 1997 to August 1999. The transect was based on measurements at 14 mooring sites extending from the western shelf break off Spitsbergen to the East Greenland Shelf break, with the deepest instruments located 10 m above the bottom. According to that figure, the magnitude of the near bottom meridional velocity in the EGCFS exceeds 2 cm s^{-1} over the lower slope and at the shelf break. Therefore a reasonable estimate of V_b is 3 cm s^{-1}. Consequently, V_β must be ~6 cm s^{-1}, as inferred from an approximately equal partition of the transport in the EGCFS between bottom and relative contributions [*Foldvik et al.*, 1988; *Fahrbach et al.*, 2001].

[11] Results of calculations of the cross-isobath component of the near bottom velocity and its ratio to the along-isobath component in the EGCFS are presented in Table 1. The calculations were based on a smoothed topography and

Table 1. Cross-Isobath Component u of the Near-Bottom Velocity in the EGCFS and Its Ratio to the Along-Isobath Component v[a]

Component	H_0	H_{20}	H_{50}	H_{100}
		Site FS-1		
u, cm/s	0.416	0.425	0.496	0.554
u/v	−0.164	−0.169	−0.197	−0.221
		Site FS-2		
u, cm/s	0.125	0.128	0.152	0.166
u/v	−0.055	−0.056	−0.066	−0.072

[a]Here, u and v were calculated by projecting the annual mean velocity vectors obtained from the deepest instruments at moorings FS-1 and FS-2 from *Foldvik et al.* [1988] on the local cross- and along-isobath directions at 79°N. Columns H_0, H_{20}, H_{50}, and H_{100} present calculations based on a topography with a different degree of smoothing, as explained in the text.

the eastward and northward components of the annual mean near bottom velocity at FS-1 and FS-2 (see Table 2 of *Foldvik et al.* [1988]). The bottom depth was calculated by local averaging of the 5-min gridded Earth topography data set, ETOPO5 [*U.S. National Geophysical Data Center*, 1988], over a square about 20 km × 20 km (H_{20}), 50 km × 50 km (H_{50}) or 100 km × 100 km (H_{100}), and then subsampled on a 1° grid. The depth contours in Figure 2 are plotted from the original (unsmoothed) data set (H_0). The projection coefficients for the velocity components were calculated from depth differences on the subsampled grid and then interpolated to locations corresponding to the bottom depths $H = H_{FS\text{-}1}$ and $H = H_{FS\text{-}2}$. Since the EGCFS flows in the direction of propagation of the topographic Rossby waves, i.e., with the shallower water to the right when looking downstream, its along-isobath component is negative in the coordinate system in Figure 1. The ratio of the velocity components in Table 1 is negative because the cross-isobath component is positive (downslope). The dependence of the estimates in Table 1 on the scale of smoothing of topography is not large, with slightly smaller values of the cross-isobath component of the flow for rougher topography. The scale U_b would be above 0.4 cm s^{-1} when based on the estimates from FS-1, and above 0.1 cm s^{-1} from FS-2. A difference between the estimates from FS-1 and FS-2 may not only reflect a different position of the instruments on the slope, but also their different height above the bottom.

[12] The scale of the surface Ekman suction in the EGCFS is $W_s = 2 \times 10^{-6}$ m s^{-1}, as estimated from a long-term mean (1948–2003) distribution of the wind stress in the area (Figure 3). The distribution has been obtained from averaged monthly mean data from the National Centers for Environmental Prediction (NCEP, in Boulder, Colorado, United States) reanalysis [*Kalnay et al.*, 1996]. The scales $V_\beta = 6$ cm s^{-1}, $f_c = 1.4 \times 10^{-4}$ s^{-1}, $\beta_c = 4.4 \times 10^{-12}$ s^{-1} m^{-1}, and $D = 2000$ m, yield $W_\beta = 4 \times 10^{-6}$ m s^{-1}. Therefore the "equivalent vertical velocity" related to the planetary β effect has a comparable magnitude to the surface Ekman suction. Both Sverdrupian terms seem, however, to be an order of magnitude smaller than the topographic term. With the scale of the bottom depth variation d (Figure 1) equal to 2000 m and $l_b = 50$ km, the scale of the bottom slope ($s_0 = d/l_b$) is 0.04. This estimate and the smallest estimate of the magnitude of the cross-isobath velocity based on Table 1, i.e., $U_b = 0.1$ cm s^{-1}, gives $W_t = 4 \times 10^{-5}$ m s^{-1}.

[13] The estimates made above indicate that the vorticity balance in the EGCFS should include a bottom friction term to remain in the limit of the large-scale dynamics. With the bottom stress parameterized as in equation (11), the current should be in the ATW balance obtained for

$$W_f = W_t \gg \max(W_\beta, W_s). \tag{15}$$

The equality of the scales on the LHS of relation (15) implies that the friction coefficient depends on the degree of anisotropy of the flow in the topographic coordinates expressed by the parameter $\alpha_b = U_b/V_b$,

$$r = df_c\alpha_b. \tag{16}$$

This relationship should hold approximately for any vorticity balance to which the bottom Ekman pumping and topographic vortex tube stretching contribute at the leading order. Figure 4 shows r as a function of α_b for external parameters, d and f_c, appropriate for the EGCFS. Four particular regimes are marked on the curve. Point R_1 corresponds to a maximum value of r (≈10 cm s^{-1}) for which the flow remains anisotropic in the sense that

$$\alpha_b^2 \ll 1. \tag{17}$$

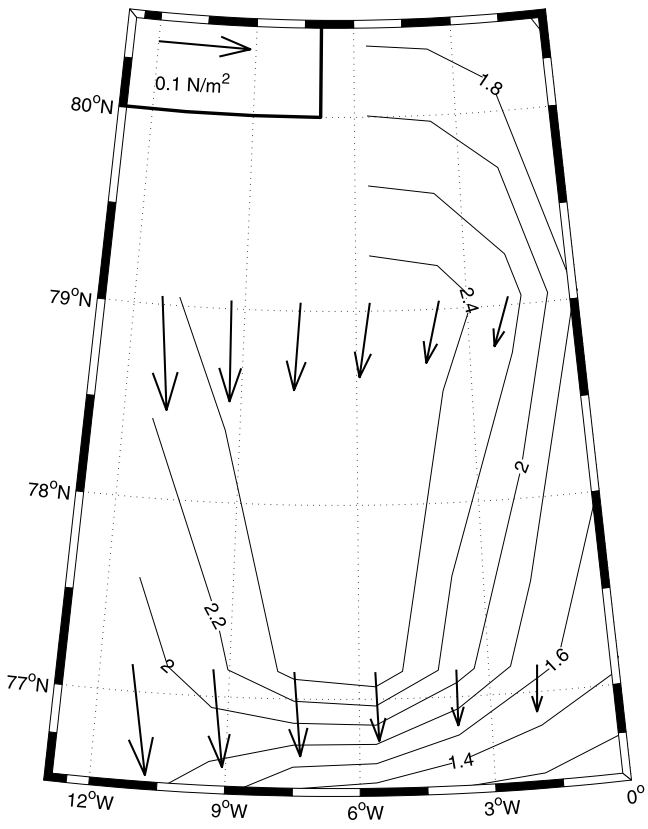

Figure 3. Distribution of the long-term mean (1948–2003) wind stress and the associated Ekman suction (in 10^{-6} m s^{-1}) in the area of the EGCFS obtained from averaged monthly mean data from the NCEP reanalysis.

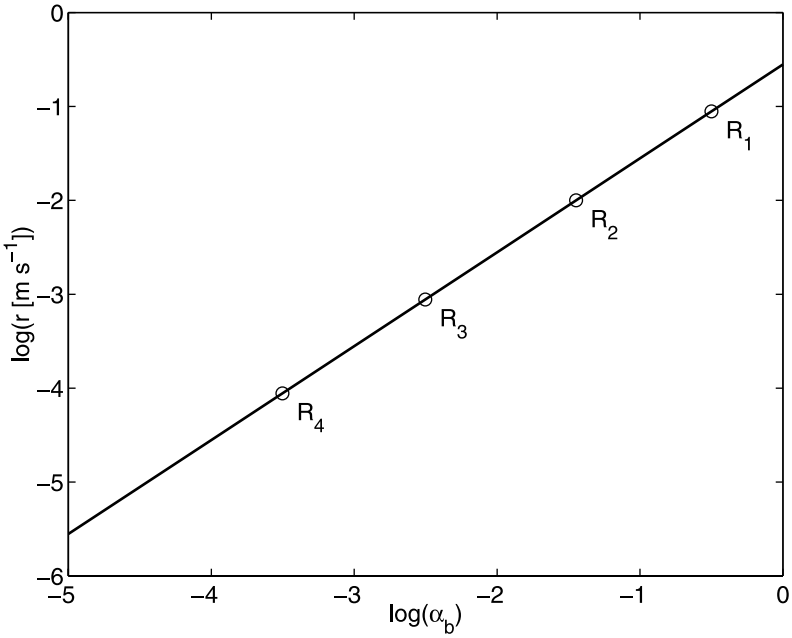

Figure 4. Friction coefficient r as a function of the anisotropy of the bottom geostrophic flow (parameter α_b) evaluated from equation (16) using the scale of the bottom depth variation (d = 2000 m) and the Coriolis parameter ($f_c = 1.4 \times 10^{-4}$ s^{-1}) appropriate for the EGCFS over the continental slope. Note that the scale of both r and α_b is logarithmic. The particular regimes R_1–R_4 are discussed in the text. The large-scale vorticity regime in the EGCFS is likely to lie between R_1 and R_2.

The somewhat arbitrary choice of the limit for α_b^2 is there 0.1. Point R_2 corresponds to the value of the friction coefficient (r = 1 cm s^{-1}) obtained for the velocity scales used in our scaling, i.e., U_b = 0.1 cm s^{-1} and V_b = 3 cm s^{-1}, for which α_b = 0.03. The ratios of the velocity components in Table 1 indicate that the value of r in the EGCFS should lie in the range between the values at R_1 and R_2. These values are larger than typical values of r found in the literature. For instance, *Csanady* [1988] cites values of 3–5 $\times 10^{-4}$ m s^{-1}. These values fall between the values at points R_3 and R_4 in Figure 4. Point R_3 corresponds to the value of r ($\approx$0.1 cm s^{-1}) for which the terms of the ATW balance would have the same magnitude as the planetary term. In the neighborhood of this point, all terms of equation (12) would significantly contribute to the vorticity balance of the EGCFS. However, such a balance would require a very small magnitude of the cross-isobath bottom geostrophic velocity, $\sim 1 \times 10^{-4}$ m s^{-1}. Such a magnitude would be appropriate also in the case of the topographic Sverdrup balance, i.e., the frictionless limit of equation (12) with a significant contribution from the topographic vortex tube stretching term. A further reduction of the value of α_b along the line in Figure 4 by 1 order of magnitude gives $r \approx 1 \times 10^{-4}$ m s^{-1} (point R_4). These values, if appropriate, would suggest the Sverdrup balance in the EGCFS. The balance is a priori not possible since w_{Es} is positive while the meridional flow is southward, so that both Sverdrupian terms have the same sign in equation (12). Both are negative. Similarly, the topographic Sverdrup balance can be ruled out on the basis of the sign of the cross-isobath flow from Table 1. A downslope motion corresponds to a topographic vortex tube stretching contributing to equation (12) a term of the same sign as the Sverdrupian terms. Therefore a large-scale vorticity balance in the EGCFS different than the frictional-topographic balance would imply that the cross-isobath bottom geostrophic velocity in the area of the sites FS-1 and FS-2 has not only a much smaller magnitude but also a different sign than the estimates in Table 1.

[14] That the friction coefficient in the EGCFS might be O(1 cm s^{-1}) is also supported by the results of the analytical and inverse modeling applied to the MIZEX 84 data. Only for such a large value of r, the magnitude of the transport in the current diagnosed from the analytical model of *Schlichtholz and Houssais* [1999c] agreed with observations. The value r = 1 cm s^{-1} was then used in the inverse model by *Schlichtholz and Houssais* [1999a]. Noteworthy is the fact that the vorticity balance could not be closed in the inverse model without friction or with r much smaller than 1 cm s^{-1}. Of course, prescribing a uniform value to the friction coefficient is an imperfect parameterization. The coefficient can be interpreted on the basis of the quadratic friction law for an instantaneous flow as

$$r = c_D V_m, \tag{18}$$

where c_D is a drag coefficient which depends on the roughness of the ocean bottom, and V_m is the speed of a high-frequency perturbation superimposed on the large-scale flow [e.g., *Csanady*, 1976, 1988]. A typical value of c_D is in the range 10^{-3}–10^{-2} according to *Csanady* [1976]. In this range of c_D, r equal to O(1 cm s^{-1}) would correspond to V_m = O(1–10 m s^{-1}), which is a too high value. According to Table 5 of *Foldvik et al.* [1988], the kinetic energy of the fluctuating part of the near bottom flow at FS-1 and FS-2 is only 2–3 times larger than the

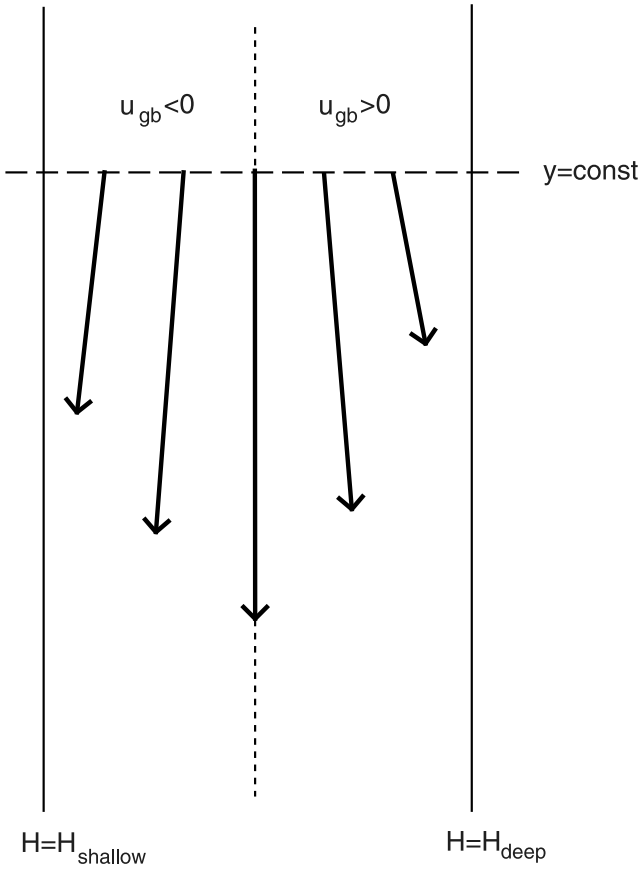

Figure 5. Schematic representation of a core of a bottom geostrophic flow in the direction of propagation of the topographic Rossby waves. H_{shallow} and H_{deep} are a shallow and deep isobaths, respectively. The cross-isobath component has the sign appropriate for the ATW vorticity balance approximated by equation (20). In the sector of a downslope (upslope) motion, the associated vortex tube stretching (squashing) should be canceled out by the bottom Ekman pumping (suction). Note that at the location of the maximum flow, the current should have other contributions to the vorticity balance than the terms of equation (20).

kinetic energy of the corresponding mean flow. With V_m = 5 cm s^{-1}, c_D should be 0.2 for r to be 1 cm s^{-1}. This implies that the "roughness" of the East Greenland Slope might be larger than suggested by the magnitude of the drag coefficient cited in studies of shallow seas or shelf circulation. Perhaps this is not surprising in view of equation (16), which shows that the friction coefficient for a slope current in the ATW balance should experience a much larger friction that a shelf current at the same latitude and with the same degree of horizontal anisotropy because of the much larger scale of the bottom depth variation.

[15] A conclusion that can be drawn from this section is that either (a) our estimates of the velocity components do not represent, even roughly, the true components of $\mathbf{u}_{gb}$ in the EGCFS, (b) the current cannot be described by the large-scale dynamics alone, or (c) the current is in the frictional-topographic vorticity balance with a relatively large drag or friction coefficient. We will assume the last alternative and further consider implications of the ATW balance. Using an approximation $f = f_c$, the balance reads as

$$f_c \mathbf{u}_{gb} \cdot \nabla H = r\hat{\mathbf{z}} \cdot \nabla \times \mathbf{u}_{gb}. \tag{19}$$

In view of relation (17), equation (19) can be reduced to a relation between the cross-isobath component of the bottom geostrophic flow, u_{gb}, and the cross-isobath variation of the along-isobath component of that flow. On a f-plane and for the bottom sloping only in one direction, i.e., $H = H(x)$, we have

$$f_c s u_{gb} = r \frac{\partial v_{gb}}{\partial x}, \tag{20}$$

where $s = dH/dx$. A downslope motion at the top of the bottom Ekman layer generates a topographic vortex tube stretching which should be canceled out by the bottom Ekman pumping. The latter, according to equation (20), corresponds to an upslope increase of the magnitude of the (negative) along-isobath velocity, as shown in Figure 5 depicting a core in the current flowing with the shallower water to the right. According to the estimates in Table 1, FS-1 and FS-2 either were both located in the sector $u_{gb} > 0$ of the schematic in Figure 5 or FS-1 was located in a shallower core while FS-2 in a deeper one. In any case, at an extreme of v_{gb}, u_{gb} should vanish for equation (20) to hold. Therefore, even if the ATW balance is dominant, there should be locations in the EGCFS where other terms come into play.

4. Divergence of the Bottom Geostrophic Flow

[16] Although the frictional-topographic vorticity balance involves the bottom geostrophic flow, it does not explicitly indicate any forcing mechanism for that flow. The latter should depend on the density distribution as it follows from consideration of the Coriolis acceleration acting on the bottom flow over a sloping bottom,

$$\hat{\mathbf{z}} \times f \mathbf{u}_{gb} = -\frac{1}{\rho_0} (\nabla p)|_{z=-H}. \tag{21}$$

The right-hand side (RHS) of equation (21) can be expressed in terms of the bottom pressure, p_b, and bottom density, ρ_b, using the identity

$$(\nabla p)|_{z=-H} = \nabla p_b + \left.\frac{\partial p}{\partial z}\right|_{z=-H} \nabla H, \tag{22}$$

and evaluating the hydrostatic equation (5) at the bottom, so that we have

$$\hat{\mathbf{z}} \times f \mathbf{u}_{gb} = -\frac{1}{\rho_0} (\nabla p_b - g\rho_b \nabla H). \tag{23}$$

Acting with the curl operator ($\hat{\mathbf{z}} \cdot \nabla \times$) on equation (23) yields

$$\nabla \cdot \left(f \mathbf{u}_{gb} \right) = \frac{g}{\rho_0} J(\rho_b, H) \equiv \text{JEBAR}_b, \tag{24}$$

where J is the Jacobian operator in the horizontal plane. By equation (24), the curl of the Coriolis force acting on the bottom geostrophic flow is maintained by along-isobath bottom density variations, an effect called JEBAR$_b$ in the introduction. On a f-plane and for the bottom sloping only in one direction (Figure 1), equation (24) is reduced to the formula for the divergence of $\mathbf{u}_{gb}$ considered by *Shaw and Csanady* [1983],

$$\nabla \cdot \mathbf{u}_{gb} = -\frac{g}{\rho_0 f_c} s \frac{\partial \rho_b}{\partial y}. \tag{25}$$

The along-isobath bottom density variations are related to the distribution of the net relative geostrophic velocity. The latter can be expressed in terms of the potential energy per unit area, $\rho_0\chi$, and the bottom density [e.g., *Schlichtholz and Houssais*, 1999c],

$$\overline{\mathbf{u}}_{gr} = \hat{\mathbf{z}} \times \frac{1}{f}\left(\frac{\nabla \chi}{H} + g\frac{\rho_b}{\rho_0}\nabla H\right). \tag{26}$$

The static density profile, ρ_r, related hydrostatically to the corresponding pressure profile, p_r, is irrelevant for the calculation. For convenience, we will treat ρ_b and χ as the anomalies with respect to their static values, i.e., $\rho_b = (\rho - \rho_r)|_{z=-H}$ and

$$\chi = \frac{g}{\rho_0}\int_{-H}^{0} (\rho - \rho_r) z dz. \tag{27}$$

Equation (26) can be rewritten as a formula for the total Coriolis acceleration acting on the relative flow,

$$\hat{\mathbf{z}} \times fH\overline{\mathbf{u}}_{gr} = -\nabla\chi - g\frac{\rho_b}{\rho_0} H \nabla H. \tag{28}$$

Now acting with the curl operator on equation (28) gives

$$\nabla \cdot \left(fH\overline{\mathbf{u}}_{gr}\right) = -H\frac{g}{\rho_0} J(\rho_b, H). \tag{29}$$

Therefore the JEBAR$_b$ can be interpreted in terms of the curl of the total Coriolis force associated with the relative geostrophic flow which, by definition, is equal to the divergence of the relative transport multiplied by the Coriolis parameter. The two quantities, JEBAR$_b$ and $\nabla \cdot (fH\overline{\mathbf{u}}_{gr})$, differ by a factor equal to the ocean depth, and have an opposite sign.

[17] The divergence of $fH\overline{\mathbf{u}}_{gr}$ can be split into planetary and nonplanetary contributions, so that

$$\text{JEBAR}_b = -\overline{\mathbf{u}}_{gr} \cdot \nabla f - \frac{f}{H}\nabla \cdot \left(H\overline{\mathbf{u}}_{gr}\right). \tag{30}$$

By equation (30), the along-isobath bottom density variations should be significant if the divergence of the relative geostrophic transport is significant and is not compensated by the advection of planetary vorticity by that transport. On a f-plane, it is the divergence of the relative transport alone which drives the bottom geostrophic flow,

$$H\nabla \cdot \mathbf{u}_{gb} = -\nabla \cdot \left(H\overline{\mathbf{u}}_{gr}\right), \tag{31}$$

as schematically depicted in Figure 1 of *Shaw and Csanady* [1983] for the case of a localized dense water formation over a sloping bottom. If the JEBAR$_b$ is not entirely compensated by the cross-isobath variation of the cross-isobath component of $\mathbf{u}_{gb}$, the scale of the flow is determined by the scale of the along-isobath bottom density variations, Θ. From equation (25), we obtain

$$V_b = \frac{g s_0}{f_c}\frac{\Theta}{\rho_0}. \tag{32}$$

To obtain estimates of baroclinic variables, the density has been computed form the annual mean temperature and salinity fields of the Polar Science Center Hydrographic Climatology (PHC, Seattle, Washington, United States). The PHC, available at the standard depth levels on a 1° horizontal grid, is a composite of two heavily smoothed climatological data sets [*Steele et al.*, 2001]. In the EGC$_{FS}$ area (see the box in Figure 2), the "effective" smoothing scale is 150–450 km and the accuracy of the density field in the deep layer is $\sim$0.01 kg m^{-3} (see Appendix A for details). The JEBAR$_b$ directly calculated from the gradients of the PHC density at the maximum unmasked standard level depth (H_{PHC}) and the gradients of $H = H_{PHC}$ is quite noisy in general. This should be at least partly attributed to a low vertical resolution of the data. Alternatively, $J(\rho_b, H)$ can be computed using the bottom depth obtained from the ETOPO5 and the PHC density interpolated or extrapolated on that depth. However, the raw version of the ETOPO5 retains small-scale variations which may be incompatible with the smooth PHC fields for a description of the large-scale dynamics. On the other hand, a large smoothing of topography requires interpolation or extrapolation of the density to depths much different from H_{PHC} which may result in an excessive along-isobath gradient of ρ_b at some locations. To test this, topographies with a different degree of smoothness (H_0, H_{20}, H_{50}, and H_{100} from section 3) have been used. A minimum root-mean-square (RMS) of $J(\rho_b, H)$ in the EGC$_{FS}$ area is obtained for H_{50}. It is smaller by 30% (3 times) than the corresponding RMS for H_{100} (H_0). The RMS of the JEBAR$_b$ for H_{PHC} slightly exceeds that for H_{100}.

[18] The distributions of ρ_b and χ for the bottom topography which most restricts the magnitude of the JEBAR$_b$ (H_{50}) are presented in Figures 6a and 6b, respectively. The distributions show a contrast between the lighter waters of the Arctic Ocean in the north and the denser waters of the Greenland Sea in the south. Both, the gradient of χ and variations of ρ_b contribute significantly to the relative flow, as shown by the distribution of the two contributions to $\overline{\mathbf{u}}_{gr}$ from equation (26) in Figure 7. The sum of these contributions results in a generally southward flow, with a magnitude of $\sim$2 cm s^{-1} (Figure 8a). Three cores of a comparable magnitude can be identified in the flow at 79°N, one over the continental slope, one at the shelf break, and another on the shelf. Consequently, the largest values of the relative

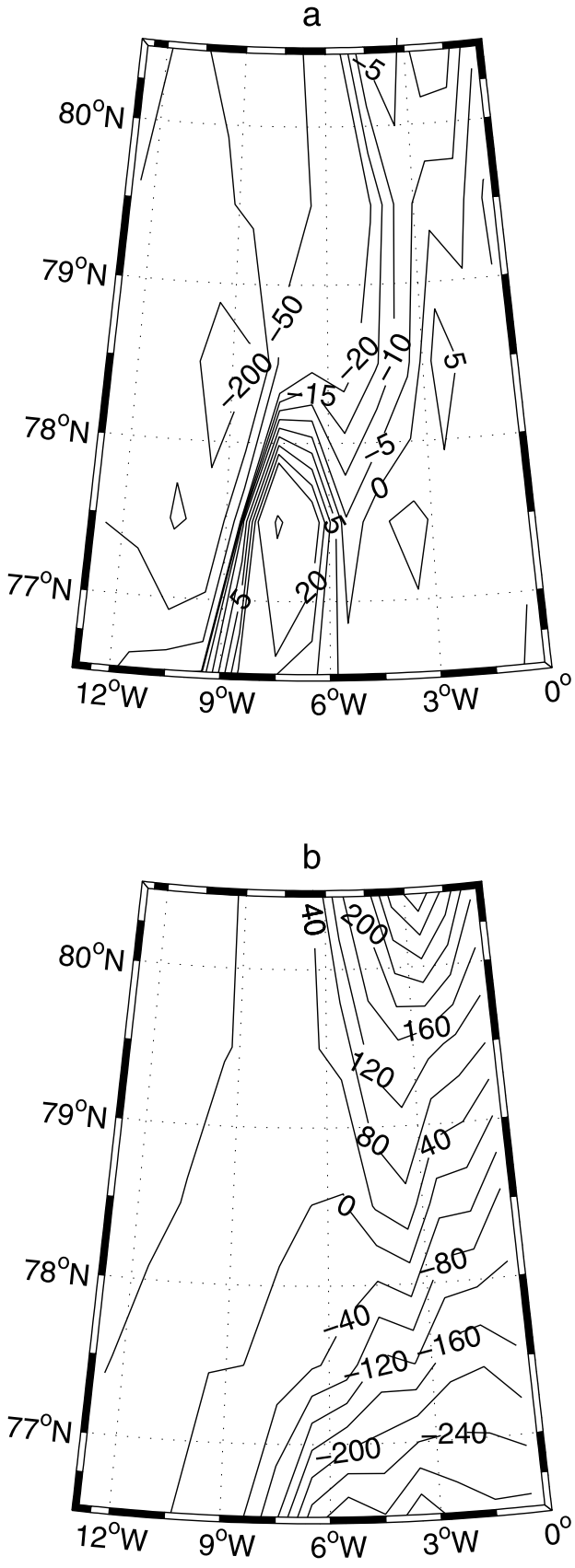

transport are found over the slope (Figure 8b). The westward flow in the southeastern part of the area represents a northern recirculating branch of the cyclonic circulation in the Greenland Sea.

[19] The divergence of the relative geostrophic transport is the main contributor to the $JEBAR_b$ in the EGCFS. The planetary contribution is 2 orders of magnitude smaller, as shown in Figure 9, where the relative magnitude of the two terms on the RHS of equation (30) is plotted as a function of longitude at 79°N. Actually, the relative transport is generally convergent. Over the slope, the convergence is $\sim 1 \times 10^{-4}$ m s^{-1} at 79°N and 2–3 times larger at 78°N (Figure 10a). By equation (29) with $f = f_c$, a convergent relative transport implies that the $JEBAR_b$ is positive (Figure 10b).

[20] Since H appears as a factor in the relationship between the $JEBAR_b$ and the divergence of the relative transport, $J(\rho_b, H)$ and $\nabla \cdot (H\bar{\mathbf{u}}_{gr})$ have a different cross-isobath distribution. At 79°N, for instance, the magnitude of $\nabla \cdot (H\bar{\mathbf{u}}_{gr})$ has a maximum over the lower slope, while the $JEBAR_b$ has a maximum at the shelf break. The location of the maximum convergence of $H\bar{\mathbf{u}}_{gr}$ on the cross-isobath section moves upslope when looking southward (Figure 10a). This shift results, for instance, in large values of $J(\rho_b, H)$ over the entire slope at 78°N (Figure 10b). Details of the distributions depend also on the degree of smoothing of topography. For instance, in the versions with no or small smoothing (H_0 and H_{20}), two maxima of the $JEBAR_b$ appear in the vicinity of the shelf break at 79°N, a stronger one on the shelf side and a weaker one on the slope side (Figure 11). A similar distribution is found for a large smoothing (H_{100}). The maximum on the upper slope disappears in the version with a moderately smoothed topography (H_{50}).

[21] The magnitude of $J(\rho_b, H)$ in the EGCFS over the slope, estimated from Figure 10b to be $\sim 2 \times 10^{-9}$ kg m^{-4} at 79°N, corresponds to a density variation of 0.01 kg m^{-3} over a distance of ~200 km. This estimate is comparable to an estimate of the variation of ρ_b along the isobath H = 2000 m obtained from quasi-synoptic data by *Schlichtholz* [2002]. According to equation (32), $\Theta = 0.01$ kg m^{-3} yields $V_b = 3$ cm s^{-1}, which is in agreement with the observations of a near-bottom flow at 79°N.

5. Analytical Solutions

[22] Observations show that the along-isobath component of a near-bottom flow in the EGCFS is larger than the cross-isobath component. We have seen in section 3 that, on the assumption of an ATW balance, the degree of anisotropy of

Figure 6. Distribution of the density anomalies in the area of the EGCFS (the box in Figure 2) obtained from the PHC climatology: (a) the bottom density ρ_b (in 10^{-3} kg m^{-3}) and (b) the potential energy χ (in m^3 s^{-2}). The anomalies were calculated with respect to the averaged density profile in the area. The climatology was interpolated or extrapolated to obtain the density at a smooth bottom, as described in the text. Note that both variables show a meridional contrast between lighter waters on the Arctic Ocean side of the area and denser waters on the Greenland Sea side.

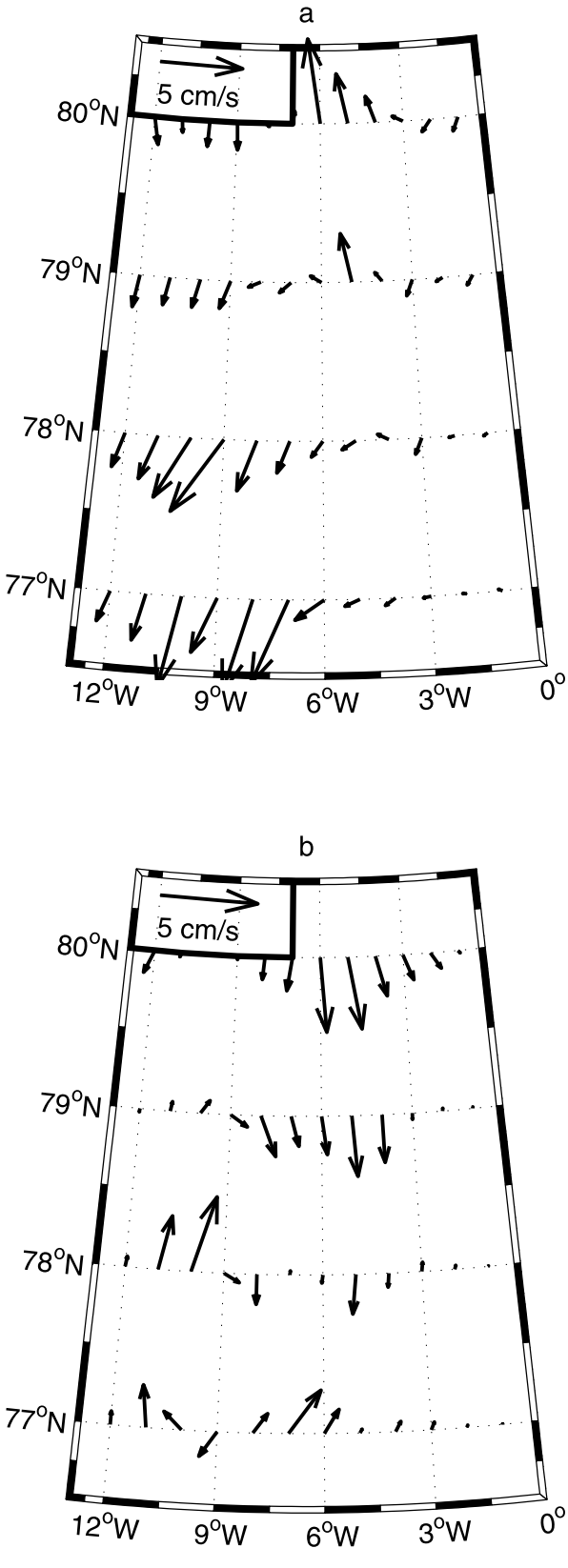

Figure 7. Distribution of the contributions to the net relative geostrophic velocity $\overline{\mathbf{u}}_{gr}$ (see equation (26)) in the area of the EGCFS: (a) the term in $\nabla\chi$ and (b) the term in $\rho_b\nabla H$. The distributions are based on the distributions of χ and ρ_b in Figure 6. Note that both contributions have a comparable magnitude.

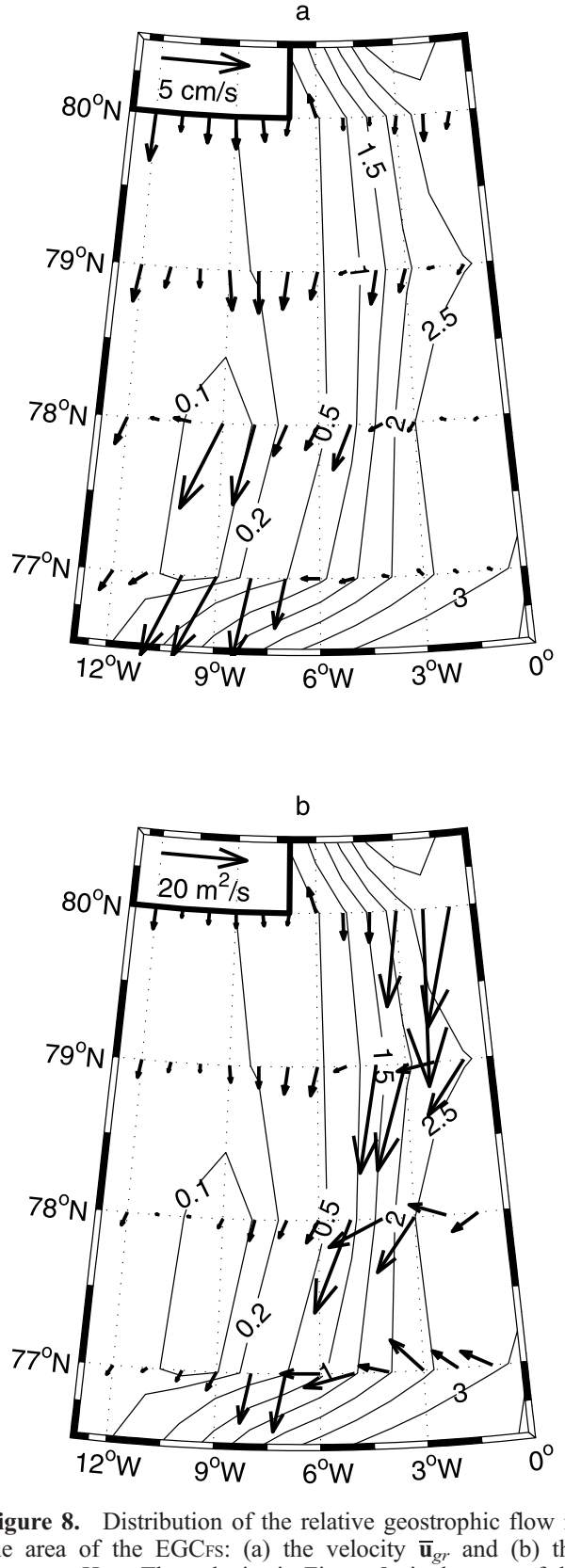

Figure 8. Distribution of the relative geostrophic flow in the area of the EGCFS: (a) the velocity $\overline{\mathbf{u}}_{gr}$ and (b) the transport $H\overline{\mathbf{u}}_{gr}$. The velocity in Figure 8a is the sum of the contributions from Figure 7. The isolines represent the bottom topography (in kilometers) used in the calculations (H_{50}). Note that the flow at 79°N occurs in three cores of a same magnitude, so that the transport is the largest in the core on the continental slope.

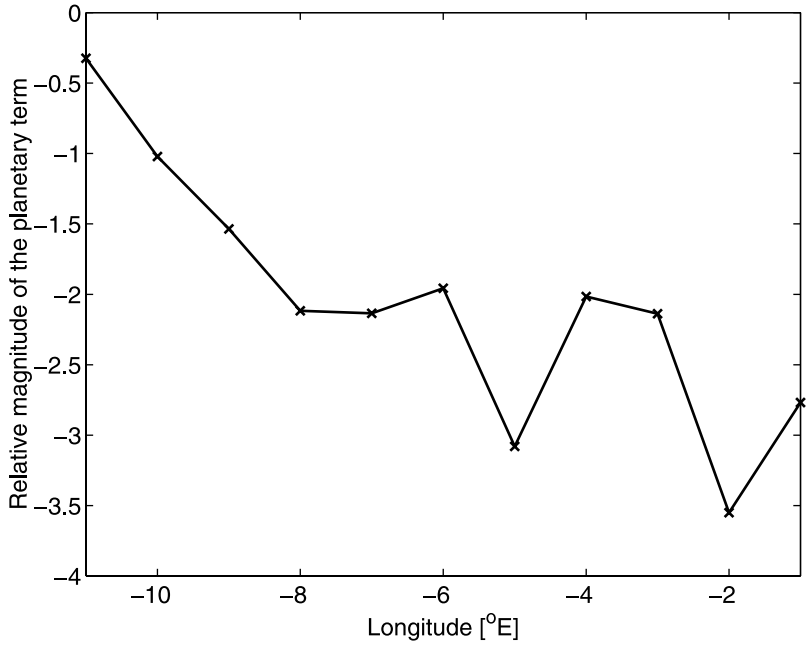

Figure 9. Distribution of the logarithm of the ratio of the planetary contribution $-\overline{\mathbf{u}}_{gr} \cdot \nabla f$ and the contribution associated with the divergence of the relative geostrophic transport to the JEBAR$_b$ (see equation (30)) in the EGCFS at 79°N. The distribution is obtained using the relative flow from Figure 8. Note that it is mainly the divergence of $H\overline{\mathbf{u}}_{gr}$ that accounts for the JEBAR$_b$.

the flow is determined by the magnitude of the friction coefficient. On the other hand, the analysis in section 4 shows that the scale of the flow itself is determined by the magnitude of the along-isobath bottom density variations. Since JEBAR$_b$ is significant while the ATW balance is a likely vorticity balance in the EGCFS, it is judicious to combine both pieces of information to learn more about the current. Eliminating the cross-isobath component of the bottom geostrophic flow between equations (20) and (25) gives a closed equation for the along-isobath component. In nondimensional form, we have

$$\frac{\partial}{\partial x}\left(\frac{1}{s}\frac{\partial v_{gb}}{\partial x}\right)+\frac{\partial v_{gb}}{\partial y}=-s\frac{\partial \rho_b}{\partial y}. \tag{33}$$

Once equation (33) is solved for v_{gb}, u_{gb} can be obtained from equation (20). In the case of a constant bottom slope ($s = 1$), equation (33) is reduced to equation (1) with $\mathcal{A} = v_{gb}$ and $Q = \partial\rho_b/\partial y$, i.e.,

$$\frac{\partial^2 v_{gb}}{\partial x^2}+\frac{\partial v_{gb}}{\partial y}+\frac{\partial \rho_b}{\partial y}=0. \tag{34}$$

[23] Consider equation (34) in a domain limited in the cross-isobath direction by $0 < x < 1$ ($0 < x < l_b$ in dimensional units, Figure 1). The problem is an analog of the problem of heat conduction in a slab, i.e., a solid bounded by two parallel planes [*Carslaw and Jaeger*, 1959]. The baroclinic "source" term acts here on v_{gb} as the internal heat source acts on the temperature of the slab. If along-isobath density variations are not zero only in the "backward" portion of the region ($y > 0$), their effect on the "forward" portion ($y < 0$) should translate into a prescribed distribution of v_{gb} at an "initial" section ($y = 0$), $v_0(x)$. In general, v_0 is a result of all physical phenomena in the "backward" region as the temperature distribution in a conducting body at an initial time is a result of past events. A mathematically analogous problem, but in a semi-infinite domain in x, was analyzed at length by *Csanady* [1978]. If we here assume that v_{gb} vanishes at the edges $x = 0$ and $x = 1$ of the "forward" region, the distribution of v_{gb} at $y < 0$ resulting from an inflow (negative v_0) or outflow (positive v_0) alone is obtained by solving equation (34) with

$$\frac{\partial \rho_b}{\partial y}=0, \qquad v_{gb}|_{y=0}=v_0(x),$$
$$v_{gb}|_{x=0}=0, \qquad v_{gb}|_{x=1}=0. \tag{35}$$

The solution of the analogous heat conduction problem, i.e., with ends of a slab kept at zero temperature, is given by *Carslaw and Jaeger* [1959, p. 93]. Adapting that solution to the present problem yields

$$v_{gb}=2\sum_{n=1}^{\infty} e^{n^2\pi^2 y}\sin(n\pi x)\int_0^1 v_0(x')\sin(n\pi x')dx'. \tag{36}$$

[24] According to equation (36), the details of the "initial" distribution of v_{gb} should gradually be lost following the "forward" region in $-y$. At large distances compared to $\pi^{-2}(\pi^{-2}\alpha_b^{-1}l_b$ in dimensional units), v_{gb} should tend to zero. An implication for the EGCFS is that the flow leaving the strait to the south should be more influenced by the local conditions in Fram Strait than by the inflow along the slope from the Arctic Ocean. An indirect evidence for that is a

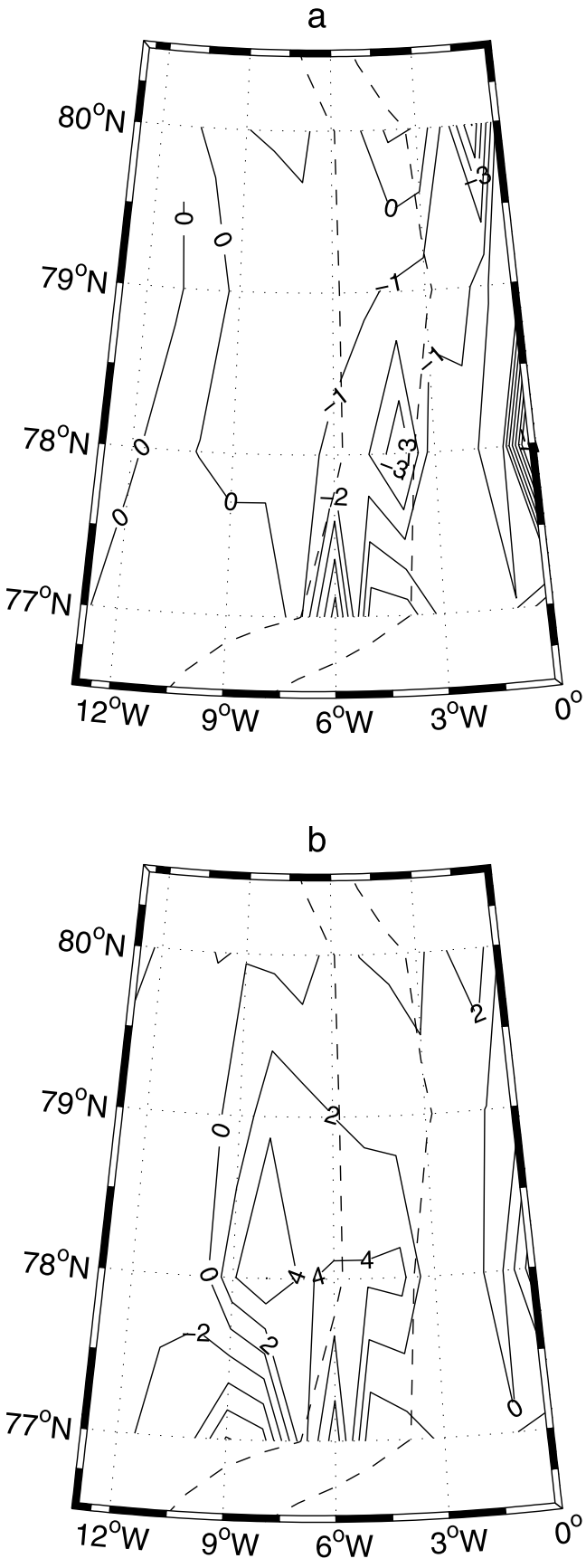

gradual change of water mass characteristics along the continental slope, already mentioned in the introduction.

[25] To find a solution in the presence of baroclinic forcing relevant for the EGCFS, take the case of a "sink" (increase of the bottom density with $-y$). Assume for simplicity that the along-isobath density variation is uniform in the "forward" region ($\partial\rho_b/\partial y = -1$), and that there is no inflow/outflow at $y = 0$. Assume also, as before, that the along-isobath flow is zero at the shallow and deep edges of the region. The problem to be solved is equation (34) with

$$\frac{\partial \rho_b}{\partial y} = -1, \qquad v_{gb}|_{y=0} = 0,$$
$$\frac{\partial v_{gb}}{\partial x}|_{x=0} = 0, \qquad \frac{\partial v_{gb}}{\partial x}|_{x=1} = 0. \tag{37}$$

The problem can be rewritten as

$$\frac{\partial^2 v^*_{gb}}{\partial x^2} + \frac{\partial v^*_{gb}}{\partial y} = 0, \qquad (0 < x < 1;\ y < 0) \tag{38}$$

with

$$v^*_{gb}|_{y=0} = \frac{x(1-x)}{2} \equiv \gamma,$$
$$\frac{\partial v^*_{gb}}{\partial x}|_{x=0} = 0, \qquad \frac{\partial v^*_{gb}}{\partial x}|_{x=1} = 0, \tag{39}$$

where $v^*_{gb} = v_{gb} + \gamma$. The equation for the auxiliary variable v^*_{gb} is homogeneous, while the "sink" term of the original problem appears in the "initial" condition for v^*_{gb}. The solution for v^*_{gb} is obtained from equation (36) with $v_0 = \gamma$. The final solution, $v_{gb} = v^*_{gb} - \gamma$, is

$$v_{gb} = \frac{4}{\pi^3} \sum_{n=1}^{\infty} \frac{e^{(2n-1)^2 \pi^2 y} \sin[(2n-1)\pi x]}{(2n-1)^3} - \gamma. \tag{40}$$

[26] The distributions of v_{gb} and $u_{gb} = \partial v_{gb}/\partial x$ are shown in Figure 12. The symmetric boundary conditions result in a symmetric distribution of both variables. The magnitude of v_{gb} has a maximum at the "midslope" position ($x = 0.5$) and increases with $-y$ at any $x = const$ except for the edges of the region, where it is zero (Figure 12a). As a consequence, u_{gb} is zero at $x = 0.5$ and, for any $y = const$, its magnitude is the largest at the edges $x = 0$ and $x = 1$ (Figure 12b). Positive (negative) values of u_{gb} on the deeper (shallower) half of the region correspond to a downslope (upslope) geostrophic motion and, therefore, to the vortex tube stretching (squashing) compensated by an Ekman pumping (suction). Since

Figure 10. Distribution of the baroclinic forcing in the area of the EGCFS: (a) the divergence of the relative transport $\nabla \cdot (H\bar{\mathbf{u}}_{gr})$ (in 10^{-4} m s^{-1}) and (b) the Jacobian of the bottom density and the ocean depth $J(\rho_b, H)$ (in 10^{-9} kg m^{-4}). The distributions are based on the same density data as Figures 6–8. The dashed lines are the isobaths $H = 500$ m and $H = 2000$ m. Note an opposite sign of the two variables and a different distribution related to the presence of the bottom depth as a factor in the relation between them (see equation (29)).

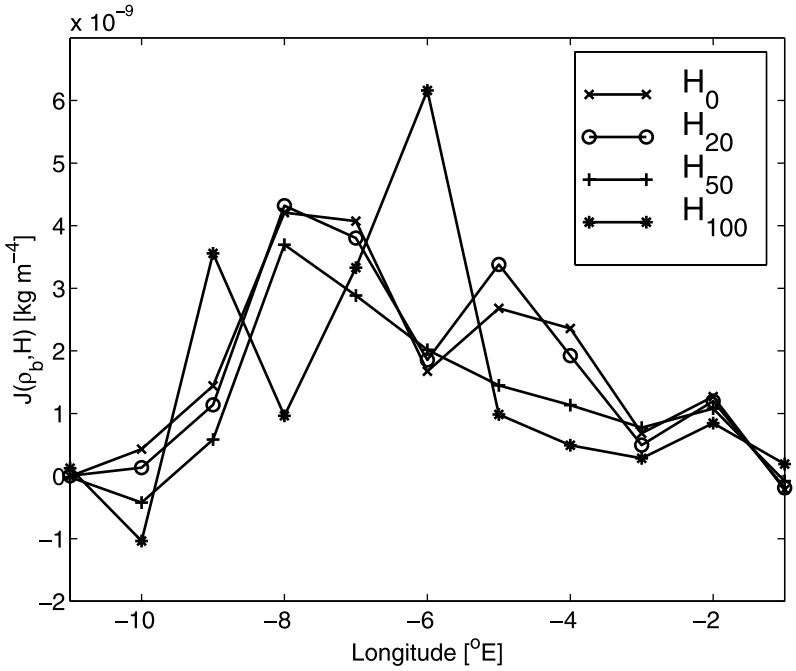

Figure 11. Distribution of the Jacobian of the bottom density and the ocean depth in the EGCFS at 79°N for different degrees of smoothing of the bottom topography. Crosses are for a rough topography (H_0), while stars are for a smooth topography (H_{100}), as explained in the text. The distribution for a relatively smooth topography (H_{50}) is a zonal section through the distribution of $J(\rho_b, H)$ in Figure 10b. Note that the latter distribution is the smoothest one and has the smallest value of the absolute maximum, which is at the shelf break (8°E).

u_{gb} is an analog of the heat flux, a positive u_{gb} at the deeper edge and a negative u_{gb} at the shallower edge correspond to a heat gain through both ends of the conducting slab. v_{gb} is negative everywhere in the ''forward'' region as should be the temperature of a conducting slab with a uniformly distributed internal heat sink and with zero temperature initially everywhere and at ends all the time. A uniform internal heat sink would reduce continuously the temperature of the slab to the moment when it would be compensated by a heat gain through the ends of the slab. Similarly, the increase of the magnitude of the along-isobath flow weakens with $-y$, so that the solution approaches a limit which is quadratic in x ($v_{gb} = -\gamma$) and corresponds to a linear change of the cross-isobath flow, i.e., $u_{gb} = x - 0.5$ at large $-y$.

[27] The above solution incorporates most essential dynamical features of the EGCFS, i.e., a southward flow and the presence of a core in the cross-isobath section. Of course, there may be more cores in the current, but there may also be local extremes in the cross-isobath distribution of the JEBAR_b (Figure 11). In addition, the forcing varies along the slope (Figure 10b), so that the real flow in the EGCFS is certainly more complex than in the simple solution. A remarkable feature of the solution is the increase of the magnitude of the flow along isobaths in the downstream direction. A southward increase of the magnitude of the bottom geostrophic flow in the EGCFS is a feature clearly appearing in the inverse model applied to the MIZEX 84 hydrographic data [*Schlichtholz*, 2002]. Of course, that feature cannot be verified by velocity observations at a single cross-isobath section. Unfortunately, the historical and present-going long-term moorings in Fram Strait are limited to a single section.

6. Discussion

[28] The analytical solutions from the previous section clearly demonstrate the importance of the JEBAR_b for flow over a frictional sloping ocean bottom. While, in the absence of that forcing, the bottom flow is gradually retarded by friction in the direction of propagation of the topographic Rossby waves, the presence of the JEBAR_b can accelerate the flow in that direction. This is likely to happen in the EGCFS under the restrictions on the validity of the ATW vorticity balance mentioned in section 3. It should also be stressed that the inference of the significance of the JEBAR_b for maintaining a divergent bottom geostrophic flow in the EGCFS, made in section 4, does not rely on particular assumptions on the vorticity balance or friction details.

[29] A question remains about the relationship between the JEBAR_b and the JEBAR. It has been shown, in section 4, that the JEBAR_b can be decomposed into a planetary term (negligible in the EGCFS) and a term in the divergence of the relative transport. The JEBAR_b can also be decomposed into a term involving the divergence of $f\,\overline{\mathbf{u}}_{gr}$ and a term involving the cross-isobath component of $\overline{\mathbf{u}}_{gr}$,

$$\mathrm{JEBAR}_b \equiv -\frac{\nabla\cdot\left(fH\overline{\mathbf{u}}_{gr}\right)}{H} = -\nabla\cdot\left(f\overline{\mathbf{u}}_{gr}\right) - \frac{f}{H}\overline{\mathbf{u}}_{gr}\cdot\nabla H. \tag{41}$$

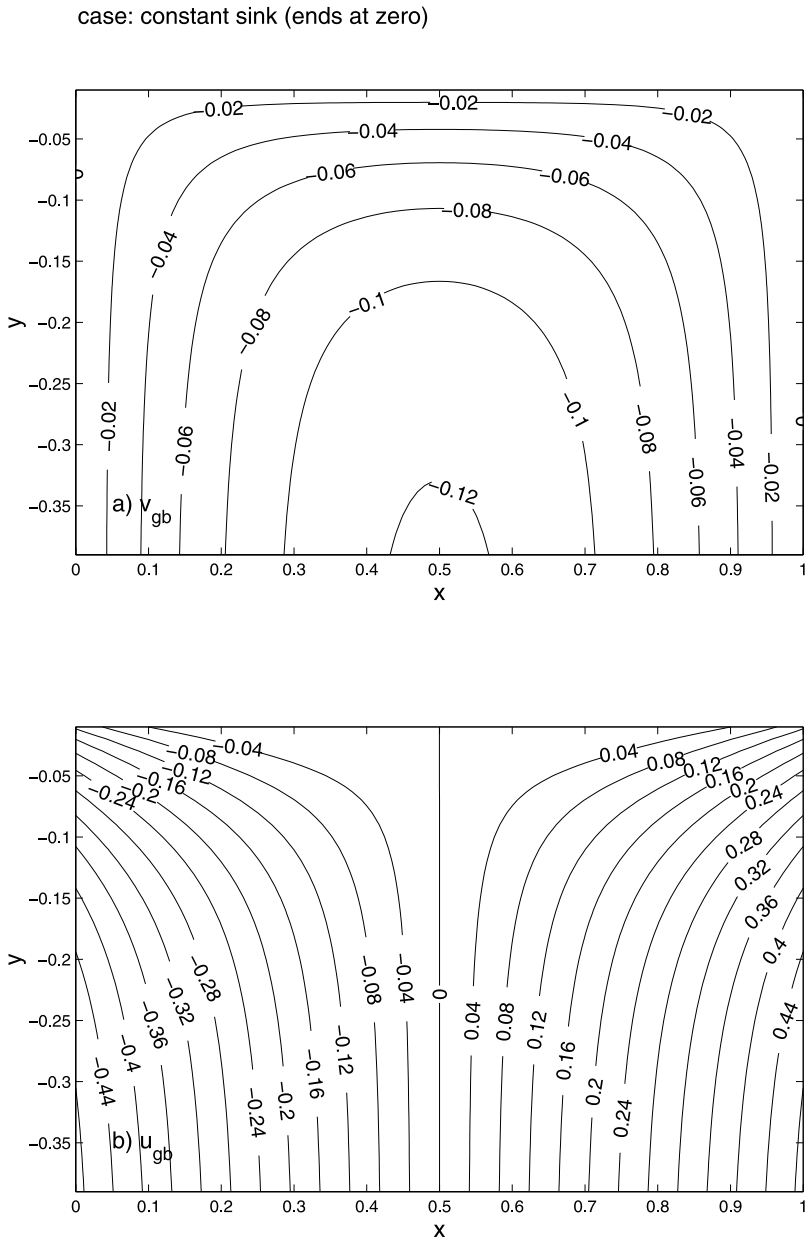

Figure 12. Divergent bottom geostrophic velocity in a density-driven current flowing over a uniformly sloping ocean bottom and satisfying the ATW vorticity balance: (a) the along-isobath component and (b) the cross-isobath component. The along-isobath component is a solution of equation (1) with $Q = const$ (a uniform $JEBAR_b$) and no inflow/outflow at $y = 0$. The sign of Q corresponds to the sign of the $JEBAR_b$ in the EGCFS. Note a gradual enhancement of the flow with $-y$ as a result of the $JEBAR_b$ forcing.

The second term on the RHS of equation (41) is the JEBAR term written in the form derived by *Mertz and Wright* [1992],

$$\mathrm{JEBAR} \equiv J\left(\chi, \frac{1}{H}\right) = -\frac{f}{H}\overline{\mathbf{u}}_{gr} \cdot \boldsymbol{\nabla} H. \tag{42}$$

Therefore the JEBAR and the $JEBAR_b$ differ from each other if the curl of the net Coriolis acceleration associated with the relative geostrophic flow is significant. We have

$$\mathrm{JEBAR} = \mathrm{JEBAR}_b + \boldsymbol{\nabla} \cdot \left(f\overline{\mathbf{u}}_{gr}\right), \tag{43}$$

which, using equation (24), yields

$$\mathrm{JEBAR} = \boldsymbol{\nabla} \cdot \left(f\overline{\mathbf{u}}_{g}\right). \tag{44}$$

So the JEBAR results from the curl of the net Coriolis force acting on the absolute geostrophic flow which, on a f-plane, is proportional to the divergence of $\overline{\mathbf{u}}_g$. This interpretation of the JEBAR was not emphasized in the literature.

[30] In the EGCFS, the JEBAR and $JEBAR_b$ are equal (or nearly so) over the continental slope, as demonstrated in Figure 13, where both terms and their difference is plotted as a function of longitude at 79°N using the climatological

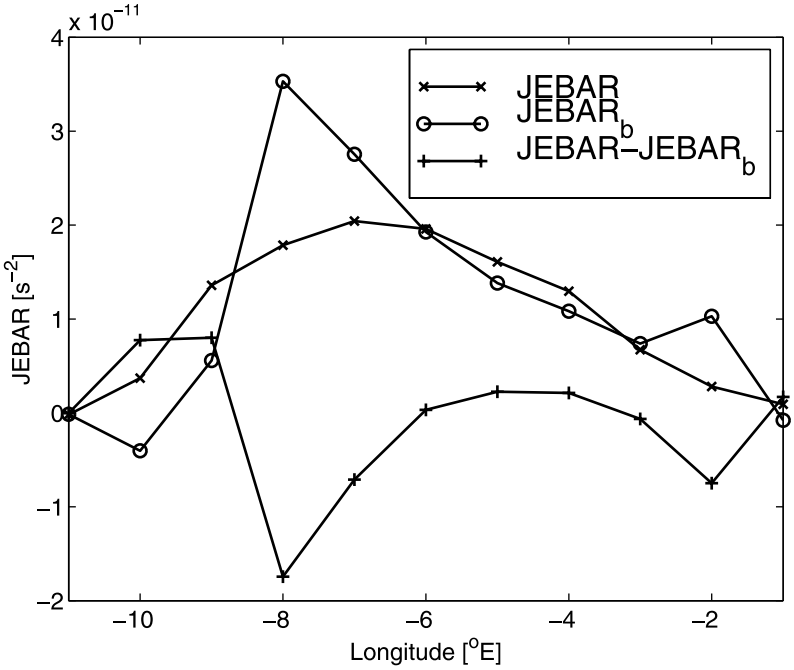

Figure 13. Distribution of the JEBAR and JEBAR$_b$ terms and their difference in the EGCFS at 79°N. A relatively smooth topography (H_{50}) has been used in the calculations, so that the JEBAR$_b$ curve is the same as the curve denoted by the plus signs in Figure 11. Note that JEBAR $\approx$ JEBAR$_b$ over the continental slope (3°–6°E) and JEBAR < JEBAR$_b$ at the shelf break and the slope base.

density distribution in the version with a smoothed topography (H_{50}). Therefore the divergence of the net geostrophic flow in the EGCFS over the slope should be achieved through the divergence of the bottom flow. The figure also shows that the divergence of the net relative flow becomes important at the slope base and, especially, at the shelf break. Answering the question whether this is a real feature or an artifact resulting from calculation of the density gradients in areas of a drastic change in the bottom slope from climatological data is beyond the scope of the study. If we assume that it is a real feature, we should conclude that the divergence of $\overline{\mathbf{u}}_{gr}$ competes with the divergence of $\mathbf{u}_{gb}$ at the edges of the continental slope since the JEBAR$_b$ is there larger than the JEBAR. However, even at the edges of the slope, the JEBAR remains positive ($\overline{u}_{gr}$ is shoreward). The overall cross-isobath distribution of the term is parabolic, with a maximum at the upper slope, where it attains a value of $\sim 2 \times 10^{-11}$ s^{-2}. The value corresponds to an increase of the magnitude of $\overline{\mathbf{u}}_g$ of $\sim$6 cm s^{-1} over a distance comparable to the latitudinal extent of the EGCFS, which is $\sim$400 km.

Appendix A: Errors of the Climatological Fields

[31] The PHC, which was intended to be a global climatology with a high-quality Arctic Ocean [*Steele et al.*, 2001], is a product of merging the 1998 version of the World Ocean Atlas (WOA) constructed from the historical hydrographic data set compiled at the U.S. National Oceanographic Data Center [*Antonov et al.*, 1998; *Boyer et al.*, 1998] with the Arctic Ocean Atlas constructed by the joint American-Russian *Environmental Working Group* (*EWG*) [1997, 1998]. The PHC retained the geometry of the WOA, i.e., the horizontal grid with nodes located at the intersection of half-degree lines of latitude and longitude and 33 irregularly spaced standard depth levels, at intervals increasing with depth from 10 m in the upper 30-m layer to 500 m below $z = -2000$ m. The merging procedure was an optimal interpolation performed on temperature and salinity fields with parameters that minimized changes to the WOA in a non-Arctic region defined as the area south of 65°N plus the Nordic Seas south of 81.5°N. Since the area of the EGCFS (see the box in Figure 2) lies within the non-Arctic region of the PHC, the PHC fields in this area closely fit the WOA fields. The RMS density difference between the PHC and WOA in the EGCFS is only 0.002 kg m^{-3} in the upper layer, at $z = -200$ m, and 0.001 kg m^{-3} in the deep ocean, at $z = -2000$ m. These values are certainly smaller than the errors of the WOA density which, however, are not well known.

[32] At each depth level, the WOA fields were obtained by correcting first-guess (or previously analyzed) values with a distance-weighted average of differences between these values and the 1°-square mean values of the raw observations at all grid points containing data within an influence area [e.g., *Antonov et al.*, 1998]. The influence radii of a Gaussian-type weight function were 888, 666 and 444 km at three successive iterations. The annual fields below (at and above) $z = -1500$ m were obtained by summing the seasonal (monthly) fields for which the first-guess values were the annual (seasonal) fields. The first-guess values for the annual fields were zonal averages of the observed data in each 1° latitude belt of individual ocean basins. A final smoothing was performed using running median and mean filters. In the EGCFS, most of data (62% at $z = -200$ m and 48% at $z = -2000$ m) were acquired from

July to September, so that the annual fields are biased toward summer conditions, especially west of the ice edge. The RMS density difference between the annual and summer fields is 0.03 kg m^{-3} at $z = -200$ m and 0.003 kg m^{-3} at $z = -2000$ m. On the other hand, the spatial coverage of the EGCFS area with available data regardless of date of observation was relatively good. For instance, at $z = -200$ m, as much as 95% of the 1° squares contained at least one observation of temperature (median = 21) and salinity (median = 14). The corresponding value for the entire World Ocean is only 63%. The discrepancy is even larger in the deep ocean where, at $z = -2000$ m, at least one temperature and salinity observation was available in 88% (42%) of the 1° squares in the EGCFS (World Ocean).

[33] According to *Olbers et al.* [1985], who analyzed an earlier version of the WOA, the statistical accuracy of the analyzed fields (σ_M) can be approximated by

$$\sigma_M = \sqrt{\frac{2}{M}}\sigma, \tag{A1}$$

where σ is the standard deviation of M independent observations contained within an "effective" radius of influence (R_e). On the basis of the wavelength of the theoretical response function of the WOA interpolation whose amplitude is reduced by 50%, R_e of ~450 km can be deduced. Then, at each grid point, σ and M can be estimated as the standard deviation and number of the 1°-square computations of the mean of the raw data used in the analysis within $R_e = 450$ km. The resulting RMS of σ_M for temperature and salinity at $z = -200$ m in the EGCFS area is 0.12°C and 0.03, respectively. The corresponding RMS values at $z = -2000$ m are 0.02°C and 0.002, respectively. These values, especially the value for the deep ocean salinity which falls below a typical instrumental error, seem unrealistically small. The value of R_e might have been overestimated or the assumption that all raw means are statistically independent may not be valid. In addition, nonstatistical errors associated with the first-guess fields may not be negligible. In any case, the above estimates are comparable to typical differences between the annual and summer fields which shows that indeed the annual means in the EGCFS are essentially summer fields. A rough idea of how large the errors of the WOA fields might be can also be obtained from inspection of the standard error of the 1°-square raw means (σ_N). At $z = -200$ m, the RMS values of σ_N for temperature and salinity are both comparable to the corresponding estimates of σ_M. However, at $z = -2000$ m, the values of σ_N are higher than the values of σ_M and correspond to a density error of ~0.01 kg m^{-3}. The values of σ_M can be adjusted to yield a density error of 0.01 kg m^{-3} by reducing R_e to 150 km. The value of 0.01 kg m^{-3} is also equal to the RMS difference between the density fields obtained from the raw and analyzed means of temperature and salinity in the deep layer. The corresponding density difference at $z = -200$ m is 7 times larger.

[34] **Acknowledgments.** The author acknowledges the computational support of the Academic Computer Center in Gdansk TASK. The Polar Science Center (Seattle, Washington, United States), the National Oceanographic Data Center (Boulder, Colorado, United States), and the National Centers for Environmental Prediction (Boulder, Colorado, United States) are acknowledged for providing hydrographic and wind stress data via anonymous ftp.

References

Aagaard, K., J. H. Swift, and E. C. Carmack (1985), Thermohaline circulation in the Arctic Mediterranean Seas, *J. Geophys. Res.*, *90*(C5), 4833–4846.

Antonov, J. I., S. Levitus, T. P. Boyer, M. E. Conkright, T. O'Brien, and C. Stephens (1998), *World Ocean Atlas 1998*, vol. 1, *Temperature of the Atlantic Ocean*, *NOAA Atlas NESDIS*, *27*, 166 pp.

Bogden, P. S., R. E. Davis, and R. Salmon (1993), The North Atlantic circulation: Combining simplified dynamics with hydrographic data, *J. Mar. Res.*, *51*, 1–52.

Boyer, T. P., S. Levitus, J. I. Antonov, M. E. Conkright, T. O'Brien, and C. Stephens (1998), *World Ocean Atlas 1998*, vol. 4, *Salinity of the Atlantic Ocean*, *NOAA Atlas NESDIS*, *30*, 166 pp.

Carslaw, H. S., and J. C. Jaeger (1959), *Conduction of Heat in Solids*, 2nd ed., 510 pp., Oxford Univ. Press, New York.

Csanady, G. T. (1976), Mean circulation in shallow seas, *J. Geophys. Res.*, *81*, 5389–5399.

Csanady, G. T. (1978), The arrested topographic wave, *J. Phys. Oceanogr.*, *8*, 47–62.

Csanady, G. T. (1988), Ocean currents over the continental slope, *Adv. Geophys.*, *30*, 95–203.

Environmental Working Group (EWG) (1997, 1998), *Joint U.S.-Russian Atlas of the Arctic Ocean* [CD-ROM], http://nsidc.org/, Natl. Snow and Ice Data Cent., Boulder, Colo.

Fahrbach, E., J. Meincke, S. Østerhus, G. Rohardt, U. Schauer, V. Tverberg, and J. Verduin (2001), Direct measurements of volume transports through Fram Strait, *Polar Res.*, *20*, 217–224.

Foldvik, A., K. Aagaard, and T. Torresen (1988), On the velocity field of the East Greenland Current, *Deep Sea Res., Part A*, *35*, 1335–1354.

Kalnay, E., et al. (1996), The NCEP/NCAR 40-yr reanalysis project, *Bull. Am. Meteorol. Soc.*, *77*, 437–471.

Mertz, G., and D. G. Wright (1992), Interpretations of the JEBAR term, *J. Phys. Oceanogr.*, *22*, 301–305.

Olbers, D. J., M. Wenzel, and J. Willebrand (1985), The inference of North Atlanctic circulation patterns from climatolgical hydrographic data, *Rev. Geophys.*, *23*(4), 313–356.

Pedlosky, J. (1996), *Ocean Circulation Theory*, Springer, New York.

Rudels, B., H. J. Friedrich, and D. Quadfasel (1999), The Arctic Circumpolar Boundary Current, *Deep Sea Res., Part II*, *46*, 1023–1062.

Sarkisyan, A. S., and V. F. Ivanov (1971), The combined effect of baroclinicity and bottom relief as an important factor in the dynamics of ocean currents, *Izv. Acad. Sci. USSR Atmos. Oceanic Phys., Engl. Transl.*, *7*, 173–188.

Schlichtholz, P. (2002), On a modified arrested topographic wave in Fram Strait, *J. Geophys. Res.*, *107*(C11), 3189, doi:10.1029/2001JC000799.

Schlichtholz, P., and M.-N. Houssais (1999a), An inverse modeling study in Fram Strait. Part I: Dynamics and circulation, *Deep Sea Res., Part II*, *46*, 1083–1135.

Schlichtholz, P., and M.-N. Houssais (1999b), An inverse modeling study in Fram Strait. Part II: Water mass distribution and transports, *Deep Sea Res., Part II*, *46*, 1137–1168.

Schlichtholz, P., and M.-N. Houssais (1999c), An investigation of the dynamics of the East Greenland Current in Fram Strait based on a simple analytical model, *J. Phys. Oceanogr.*, *29*, 2240–2265.

Schlichtholz, P., and M.-N. Houssais (2002), An overview of the θ-*S* correlations in Fram Strait based on the MIZEX 84 data, *Oceanologia*, *44*(2), 243–272.

Shaw, P.-T., and G. T. Csanady (1983), Self-advection of density perturbations on a sloping continental shelf, *J. Phys. Oceanogr.*, *13*, 769–782.

Steele, M., R. Morley, and W. Ermold (2001), PHC: A global ocean hydrography with a high-quality Arctic Ocean, *J. Clim.*, *14*, 2079–2087.

U.S. National Geophysical Data Center (1988), 5-minute gridded global relief data (ETOP05) [CD-ROM], http://www.ngdc.noaa.gov/mgg/fliers/93mgg01.html, Boulder, Colo.

P. Schlichtholz, Institute of Oceanology, Polish Academy of Sciences, Powstancow Warszawy 55, PL-81-712 Sopot, Poland. (schlicht@iopan.gda.pl)